

Understanding seasonal variations in bi-facial gain predictions by the Light Ambiance Detector in AMOLF's solar array

Photovoltaics, Bifacial Solar Cell, Seasonal Dependency, Light Detector, Diffuseness

*Bachelor Thesis
Sciences*

Kaspar Wachinger
118790245

kaspar@wachinger.org

17.07.2020
Amsterdam University College
Sciences


AUC Supervisor:
AMOLF Supervisor:
Tutor:
Reader:

dr. Forrest Bradbury
dr. Bruno Ehrler
dr. ir. Bart Verheggen
Prof. dr. Wim Sinke

f.r.bradbury@auc.nl
b.ehrler@amolf.nl
b.verheggen@auc.nl
wim.sinke@tno.nl

5764 Words

Abstract

 This paper aims to provide an understanding of seasonal, site-specific bi-facial gain variations. Investigating impacts of reflections, sun angle, and albedo on bi-facial gain allows an estimation of bi-facial solar cell performance prior to application. Analyzing the data collected by an omnidirectional light sensor setup at the AMOLF institute, Amsterdam, the bi-facial gain throughout the year 2019 was calculated. This provided the basis for determining small-scale impacts of weather and reflections on the bi-facial gain. Weighted averages resulted in a more general seasonal performance evaluation. A higher overall bi-facial gain percentage was evident in summer, in particular during dawn and dusk. Reflections, as well as season-specific weather events, such as snow, could be linked to spikes in bi-facial gain.

Abbreviations

BFSP	Silicon bi-facial solar panel
MFSP	Silicon mono-facial solar panel
LAD	Light ambiance detector
RE	Renewable energy
CSV	Comma-separated value list
BFG	Bi-facial Gain
RGB	Red, green, and blue light
IR	Infrared light
AM	Air mass

Table of Contents

1. Introduction	4
2. Methodology.....	5
2.1 Light Ambience Detector.....	6
2.2 Calibration and conversion.....	7
2.3 Data Analysis	8
2.4 Plotting	12
3. Results	12
3.1 Irradiance Comparison.....	12
3.2 BFG in 2019	12
3.3 Summer and Winter Solstice.....	15
3.4 Sun Angle Impact on BFG	18
3.5 BFG Day Weighted Average.....	22
4. Discussion	25
4.1 Reflection on data Analysis	25
4.2 Limitations.....	27
5. Conclusion.....	30
6. References	31
7. Appendix.....	32
8. Acknowledgements	33

1. Introduction

The climate crisis alerts us to the necessity of transitioning to **renewable energies (RE)**. For the continued efforts towards an ideal energy transition, wind energy and photovoltaics (i.e. solar energy) currently appear to be the most promising alternatives to nuclear or fossil energy. Due to the projected drastic increase of global demand for photovoltaics over the next decade [1], improving current commercial options will result in an overall increase in global RE share.

The increase of solar cell¹ application in unconventional areas such as wall fronts, roads etc., suggests the necessity of innovative solar panels beyond the scope of conventional photovoltaics. **The vast majority of our surroundings are not directly illuminated, but are illuminated by indirect² sunlight, due to influences by the atmosphere, clouds, surrounding objects, and surface albedo.** Conventional, mono-facial solar panels (MFSPs) rely solely on light exposure from the direction they are facing, whereas bi-facial solar panels (BFSPs) can absorb light from both sides, resulting in an overall increase of efficiency [10]. MFSPs usually have a reflective back cover and a contact back plate or **an absorbing back sheet in a bright color**. Figure 1 shows a BFSP of **surface height H** exposed to direct sunlight, diffuse sunlight, and surface albedo [10]. The contribution of the latter is almost entirely lost in conventional MFSP application.

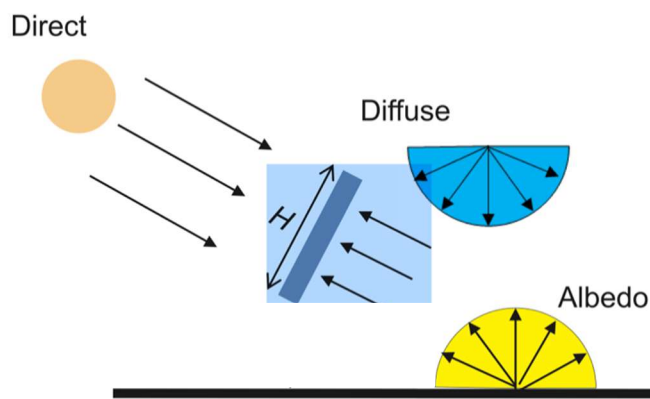


Figure 1: Irradiance factors a BFSP (blue) of surface height H is exposed to. Arrows represent incident direction of light.

¹ All solar panel technologies described in this thesis are Silicon-based photovoltaics with its specific bandgap of 1.12eV [2]

² For this paper defined as all non-direct radiation from the sun (including diffused and refracted light)

BFSP in particular, is a technology which is proven to be feasible at a considerably low additional cost compared to MFSP [7]. To make BFSP more attractive, further research into quantifying the location-specific advantages of BFSP is required. Some modelling has been done to evaluate BFSP potential in specific geographical regions [6] [4], however without extensive data sets that stretch long periods of time.

The efficiency of silicon-based photovoltaics depends on various factors, such as temperature of the cell and its surroundings, which vary throughout the year [9]. As an example, precipitation and cloud cover is inherently higher in winter, which results in increased light diffusion: Under these circumstances, most power is generated by the solar cell through photons indirectly reaching the surface of the panel suggesting an increased percentage of power generated by a BFSP, relative to a MFSP. In a research collaboration with AMOLF,³ this study aims to investigate the fluctuations in efficiency advantage of BFSP over MFSP throughout the year. The three main factors which seem likely to motivate this fluctuation were investigated: Change in sun angle throughout the year, irradiance both sides of the BFSP would receive relative to each other, and the reflectivity (including albedo) of the surroundings. It is worth noting that logically both sun angle and surrounding reflectivity have an impact on the measured irradiation.

2. Methodology

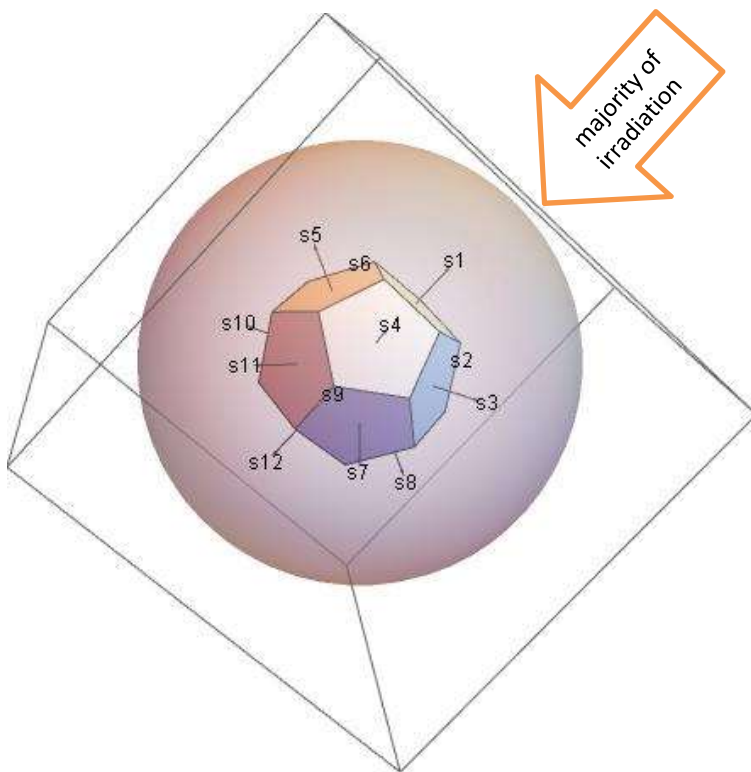
This thesis continued the research conducted by Andrea Pollastri (2019) at AMOLF [8], with the goal of evaluating the seasonal fluctuations of relative bi-facial gain of BFSP over MFSP, as well as the contribution of the individual factors which will be elaborated upon in this section. Data of the whole year of 2019 was analysed in several steps. To understand the methodological steps of data analysis, the location specific data capture elements are explained below.

³ the FOM-research institute for physics of functional complex matter (Science Park, Amsterdam)

2.1 Light Ambience Detector

The majority of data used for this thesis was captured by a light diffusion measurement tool prototype, the Light Ambience detector (LAD), located at the AMOLF solar array (see Appendix a). The LAD was developed and installed by AMOLF during project collaborations with Bachelor Students in 2018 [6][8]. The LAD is a dodecahedral body enclosed in two pmma⁴ hemispheres, with light sensors on each of the twelve sides. The Irradiation measured at the front and the back⁵ sensor of the LAD is used to estimate the efficiency of a BFSP in comparison to MFSP. Since measurements were taken at five-minute intervals for the whole year of 2019, fluctuations in both total irradiance and irradiance ratio can be investigated.

Figure 2 below is a visualization of the LAD and the sensor positions on the surfaces of the dodecahedron. The LAD was positioned in such a way that direct sunlight came from the indicated direction at most times. Picture 1 is a picture of the LAD in June 2020.



Picture 1: LAD, 17.06.2020, 11:30
Minor condensation is visible (see section 4.2)

Figure 2: LAD 3D Visualization [8].
s1 - s12 point at the position of sensors 1 to 12
and their orientation relative to each other

⁴ PMMA (acrylic) is a type of plastic

⁵ Front is defined as sensor 1 in Figure 2, facing towards the sun back is defined as sensor 12, located on the opposite side.

The diodes contained in each of the light sensors on the LAD measure red (R), green (G), blue (B), and infrared (IR) light every five minutes. Taking the arithmetic mean of the RGB and IR values at a given point in time yields the amount of irradiation (in W/m^2) reaching the sensor.

The raw data output of six commercially available solar cells⁶, weather station⁷, LAD and spectroradiometer⁸ located in front of AMOLF, science park, was automatically captured and saved to the local storage unit every 5 minutes. This data is collected and formatted into consolidated monthly reports (so called "Masterlists"). The Masterlists for January until December 2019 provide the basis for this research.

The Monthly Masterlist groups all the captured raw data in CSV format, corresponding to the day, month, year, time, and absolute timestamp (seconds since 01.01.1900). For the data analysis of this paper, only a fraction of the total Masterlist was relevant. All solar panel parameters and spectroradiometer data were not relevant, since the LAD was tested as a self-sufficient measurement tool assisting in ambient light modelling. Precipitation measurements of the weather station are occasionally considered to support hypotheses about weather fluctuations.

2.2 Calibration and conversion

The sensor calibration method performed by Pollastri (2019) was based on measurements of all 48 diode's responses to different illumination levels from a solar spectrum simulator⁹, each taken with several different temperatures [8]. The resulting Calibration function was improved using a more rigorous model, analysis, and uncertainty estimation [11]. The resulting updated conversion script provides the base of data calibration and conversion on which the data analysis of this research was grounded.

⁶ The AMOLF solar cells are: a) copper indium gallium selenide (CIGS) panel, b) cadmium telluride (CdTe) panel, c) multicrystalline silicon (PolySi) panel, d) integrated back-contact monocrystalline silicon (IBC Si) panel, e) heterojunction intrinsic layer monocrystalline silicon (HIT Si) panel, f) copper indium gallium selenide (CIGSm) panel with back mirror. [AMOLF Datasheet]

⁷ measuring precipitation, wind direction and speed, air pressure, and humidity

⁸ The AMOLF MS-711 Spectroradiometer measures irradiance values, between 300 and 1100nm, with a field of view of 180°

⁹ The solar simulator has a 1.5G air mass filter, which resembles the typical AM1.5 global radiation spectrum, which is the standard spectrum at the Earth's surface.

2.3 Data Analysis

All data analysis was performed using Wolfram Mathematica (version 12.1.0.0). The code and all analyzed data were uploaded to a permanent drive.¹⁰

Since it is desirable to only consider daytime data, meaning data during times when a BFSP would generate electricity, zeroes and/or holes in the Masterlists were removed from the dataset pre analysis. To avoid distortion of the upcoming average calculations, all **holes** and zeroes from the dataset containing converted LAD measurements were also removed. More specifically, the criterion for whether a timestamp and the corresponding datapoints would remain in the list was defined as follows: if the converted value of any of the eight front or back facing RGB and IR diodes was zero, then the datapoint was removed. This resulted in monthly lists of daytime data which were tested against the time of sunrise and sunset, matching each other within a tolerance window of 15 minutes on ten test days. The two major holes in the data of 2019 aside, which are discussed in detail later on (see section 4.2 *Limitations*), this approach to daytime calculation proved to be consistent and precise.

The results of the data analysis were evaluated in the context of seasonal variations. The four seasons were defined as follows:

- Winter: 1st of December until 28th of February
- Spring: 1st of March until 31st of May
- Summer: 1st of June until 31st of August
- Fall: 1st of September until 31st of November

For seasonal evaluation, datapoints of the days and/or weeks immediately around summer solstice, winter solstice, spring equinox, and fall equinox¹¹ were used to maximize differences in the position of the sun. **The potential distortion effect** of December 2019, which technically belonged to the winter of January and February 2020, was not considered, because general seasonal fluctuations were investigated, and not the fluctuation specific to the winter of 2018/2019.

¹⁰ <https://drive.google.com/drive/folders/1pomnKZ8Hk7VFPLgUC3w-a4u8c37wMEE5?usp=sharing>

¹¹ June 2nd, December 21st, March 20th, and September 23rd respectively

Irradiance

The irradiance each sensor was exposed to every five minutes, was measured by the four diodes of each sensor board. The calibration process, using a solar simulator, assumes that each of the four diodes were subjected to a light of spectral dependence matching the AM1.5 global radiation spectrum both during outside application and during the calibration process. The former is only approximately true, since various factors such as weather conditions and sun angles result in variations of spectral contributions. Because continuing the previous approach by Pollastri [8] (i.e. summing the irradiance of all four diodes for each data point) would result in an overestimation of the total irradiance by a factor of approximately four, a simple average of the irradiance measured across the four diodes is determined.

$$\text{Total Irradiance:} \quad I = \frac{\text{Red} + \text{Green} + \text{Blue} + \text{Infrared}}{4} \quad (1)$$

As the irradiance contribution analysis by Pollastri [8] has shown, considering only the front and the back sensor on the LAD, as opposed to utilizing the six sensors in direction of the front and the back hemisphere, yields a more accurate estimation basis of BFSP performance. This is considered a relative improvement in accuracy to a twelve-sensor approach but not optimizing modelling accuracy overall. The estimation allows for an investigation of how a typical optimal south-facing angle for a BFSP will perform. The LAD's extra sensors will hopefully eventually be integrated into a more elaborate model for predicting BFSP performance with arbitrary orientations.

In addition to increased accuracy of individual sensor irradiance, using only sensor 1 and sensor 12 represents solar panel performance more accurately. This is primarily due to the matching 180-degree field of view of the sensor, in accordance with the same field of view either side of a BFSP would have. Additionally, reflectivity of the protective layer in the light sensor can be assimilated to the reflectivity of the top protective cover in a solar panel. The irradiance of front and back sensor was calculated for the data of January until December 2019 to generate a CSV list with the respective timestamps.

Bi-faciality factor

A BFSP will not reach the same efficiency on each face, since the contact grid on one side will block some of the sunlight. The factor of performance which relates the less efficient side to the more efficient side is called the bi-faciality factor. The value of the bi-faciality factor would be zero for a MFSP with a full back sheet. For typical BFSP, a bi-faciality factor of 0.8 was assumed, matching the bi-faciality factor in site-specific previous research [4].

$$\text{Bi faciality factor:} \quad b = 0.8 \quad (1)$$

Bi-facial solar panel irradiance ratio

To visualize the performance of BFSP relative to MFSP, and minimizing measurement uncertainty, the ratio of Irradiance a BFSP is exposed to relative to a MFSP was calculated. This equation includes the bi-faciality factor, as it models the performance of a BFSP instead of the actual irradiance the back sensor received.

$$\text{BFSP Irradiance Ratio:} \quad BIR = \frac{\text{Irradiance front} + \text{Irradiance back} * b}{\text{Irradiance front}} \quad (2)$$

Bi-facial gain (BFG)

The ratio in equation (2) is readily simplified when considering only the gain a BFSP would allow relative to a MFSP. This percentage indicates the efficiency increase of a BFSP relative to a MFSP and will be referred to as bi-facial gain (BFG).

$$\begin{aligned} \text{Bi-facial gain:} \quad BFG &= BIR - 1 \\ BFG &= \frac{\text{Irradiance back} * b}{\text{Irradiance front}} \end{aligned} \quad (3)$$

Weighted Average Gain

The BFG and the BFSP Irradiance Ratio do not reflect the actual power generated. The LAD is used as a tool to model performance, independent of solar cells positioned in the vicinity, and thus no actual power output assumptions are made. A weighted gain average, however, can be calculated to incorporate the total

irradiance the hypothetical BFSP would have been exposed to. This Weighted average is calculated for each five-minute (300 seconds) interval. Since all successful measurements are five minutes apart, dividing the exposure sum of front and back will cancel the interval sum and allows to discuss an “energy” gain percentage for BFSP.¹²

Weighted average Gain:

$$WG = \frac{\sum_{t_0}^t (Irradiance\ back * b * 300s)}{\sum_{t_0}^t (Irradiance\ front * 300s)}$$

$$WG = \frac{\sum_{t_0}^t (Irradiance\ back * b)}{\sum_{t_0}^t (Irradiance\ front)} \quad (4)$$

Calculating the weighted average gain will aid in understanding potential seasonal fluctuations, as it can remove the noise resulting from other momentary events which are further elaborated upon in Figure 3. The main factors resulting in BFG fluctuations, which are assumed to regularly occur at the AMOLF solar panel, are listed relative to their impact.

BFG increase	BFG decrease
Low sun angles (potentially hitting the backside)	High sun angles
Increased albedo (Snow, changing color of grass, etc.)	Shade of the BFSP itself ¹³
Reflection (surrounding buildings, windows, etc.)	
Weather changes increasing diffusivity of ambient light (clouds, rain, etc.)	
Other environmental light sources (car lights, streetlights, etc.)	
Specific light modification (dirt cover, condensation, etc.)	

Figure 3: BFG impact classification of factors

¹²it may need to be pointed out that the surface area on both sides of BFSP is equivalent per definition.

¹³ At AMOLF, this is analogous to the shade of the solar array on which the LAD is mounted

2.4 Plotting

All plots were created with the Wolfram Mathematica ListPlot function, using custom ranges when ignoring major spikes in the visualization.

3. Results

3.1 Irradiance Comparison

The following graph shows the irradiance of the back sensor and the front sensor measured for each five-minute interval during the daytime of the year 2019.

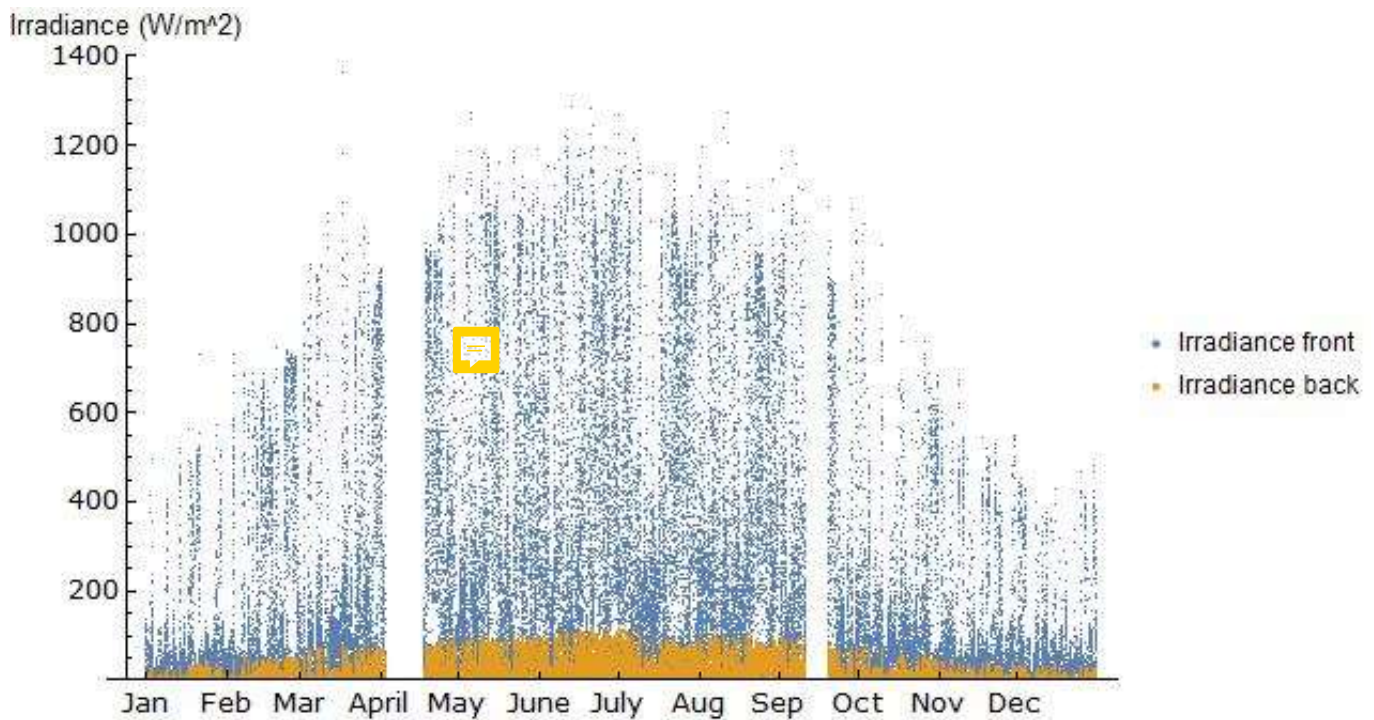
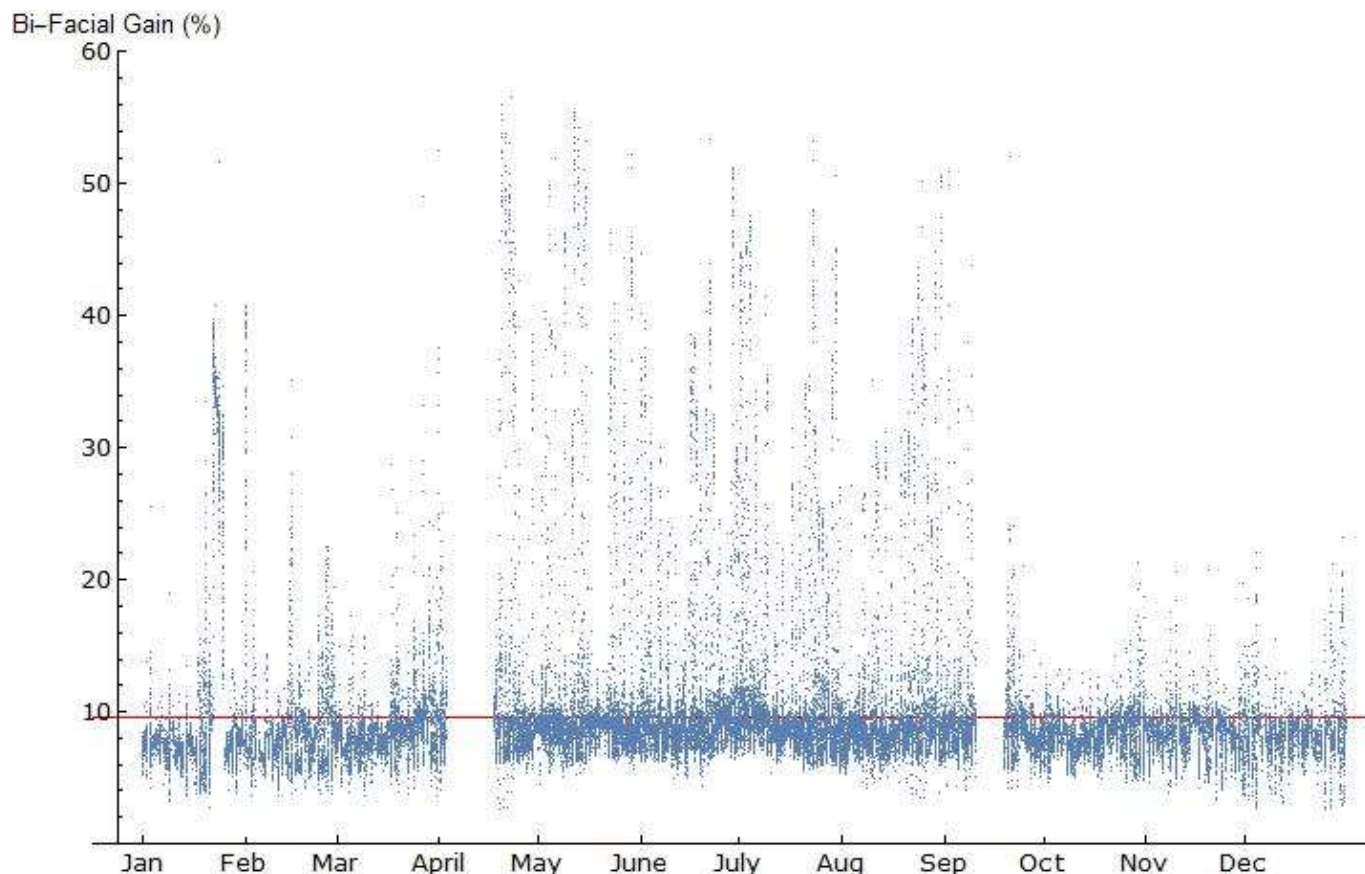


Figure 4: Irradiance front and back for 2019

Calculation of the arithmetic mean, comparing the irradiance in winter to irradiance in summer, showed that the front sensor received 36.9% of summertime irradiation during the winter months. For the back sensor this was 30.6%.

3.2 BFG in 2019

Plotting the BFG in percentages throughout the year in Figure 5 aims to shed light at the actual distribution of high BFG.



*Figure 5: BFG for all successful measurements in 2019.
The red line at 9.5% represents arithmetic mean of all blue markers.*

A small, but noticeable curved trend, which is lower in January and December, can be seen in the cluster line containing most of the 2019 data points. The BFG arithmetic annual mean of 9.5% was added as the red line, visualizing how the BFG exceeds this average less frequently in winter than in summer. Furthermore, the peaks of this list plot indicate an occasional site-specific BFG of 59%.¹⁴ These high gains occur more frequently in summer. To better understand the conditions under which high BFG occurs, we plot the front irradiance relative to the BFG for all datapoints in 2019, as seen in Figure 6.

¹⁴Disregarding the observation of disproportionally high and very rare BFG peaks of up to 81%.

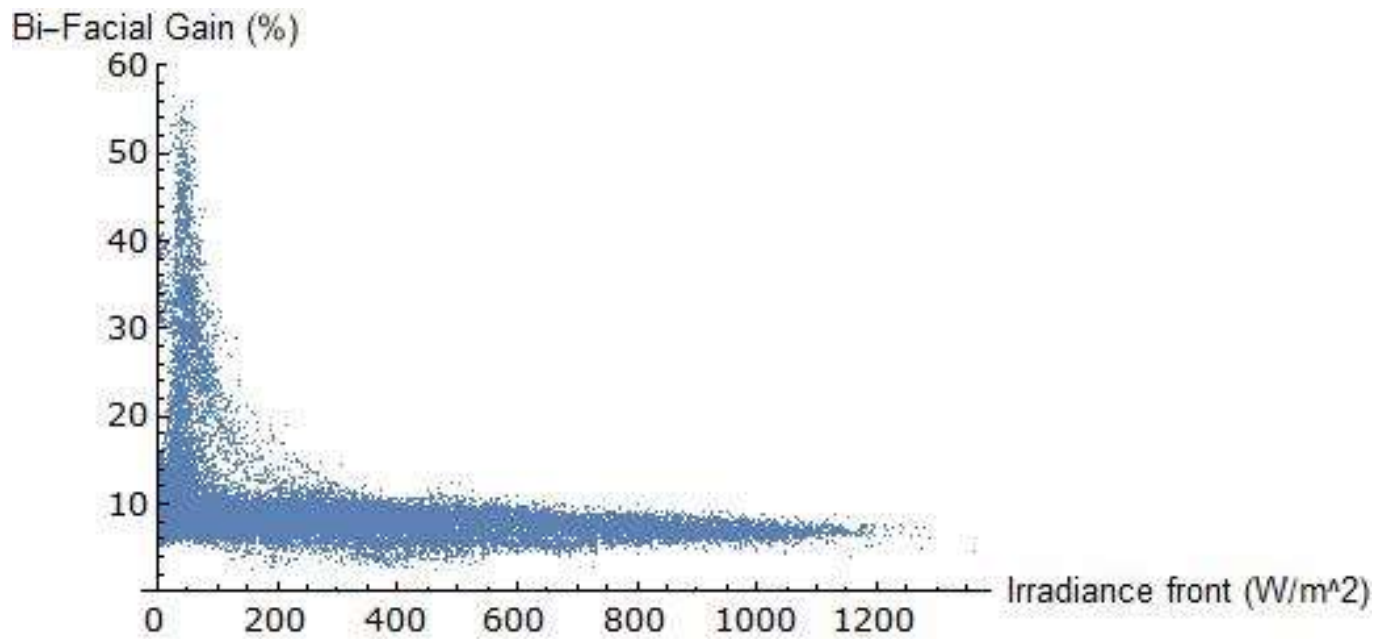


Figure 6: BFG in 2019 relative to the coinciding front irradiance

For irradiances higher than 400 W/m², the BFG was never above 15%. It is an evident trend that high BFG coincide only with lower irradiances. Bearing in mind that Figure 5 suggests an increased frequency of BFG peaks during the summer months, these BFG peaks must mostly occur especially in these hours in summer, when irradiances are low, which is during morning and evening hours.

3.3 Summer and Winter Solstice

To minimize noise, the week of summer solstice and winter solstice were used as samples during opposite times of the year. Figure 7 - 10 show the Irradiance and the BFG during the solstice test weeks.

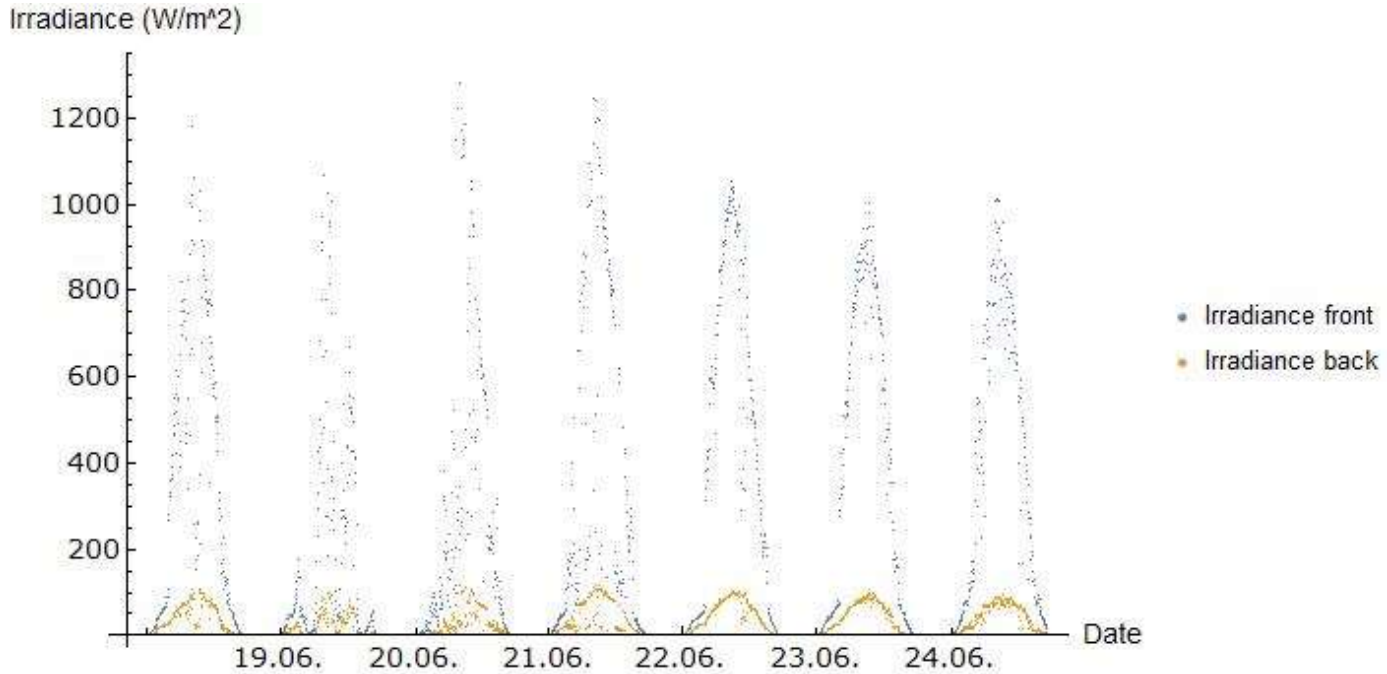


Figure 7: Irradiance front and back for the period of 18.06.2019 until 24.06.2019

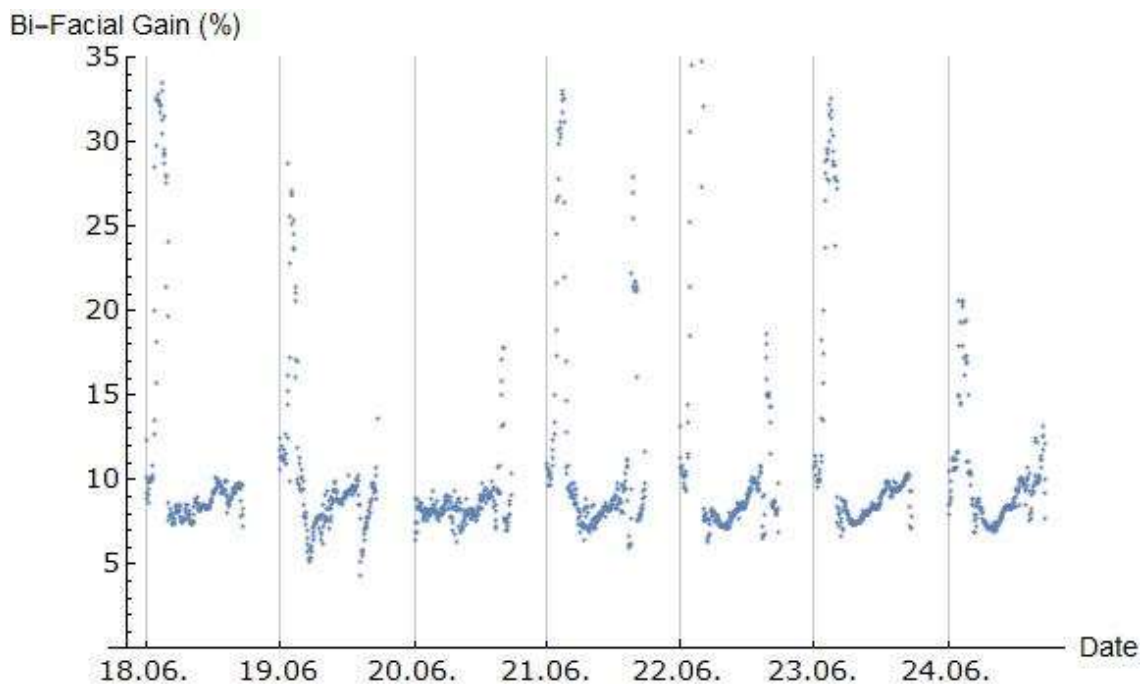


Figure 8: BFG for the time period of 18.06.2019 until 24.06.2019.
The vertical lines mark the first measurement of each day (at dawn)

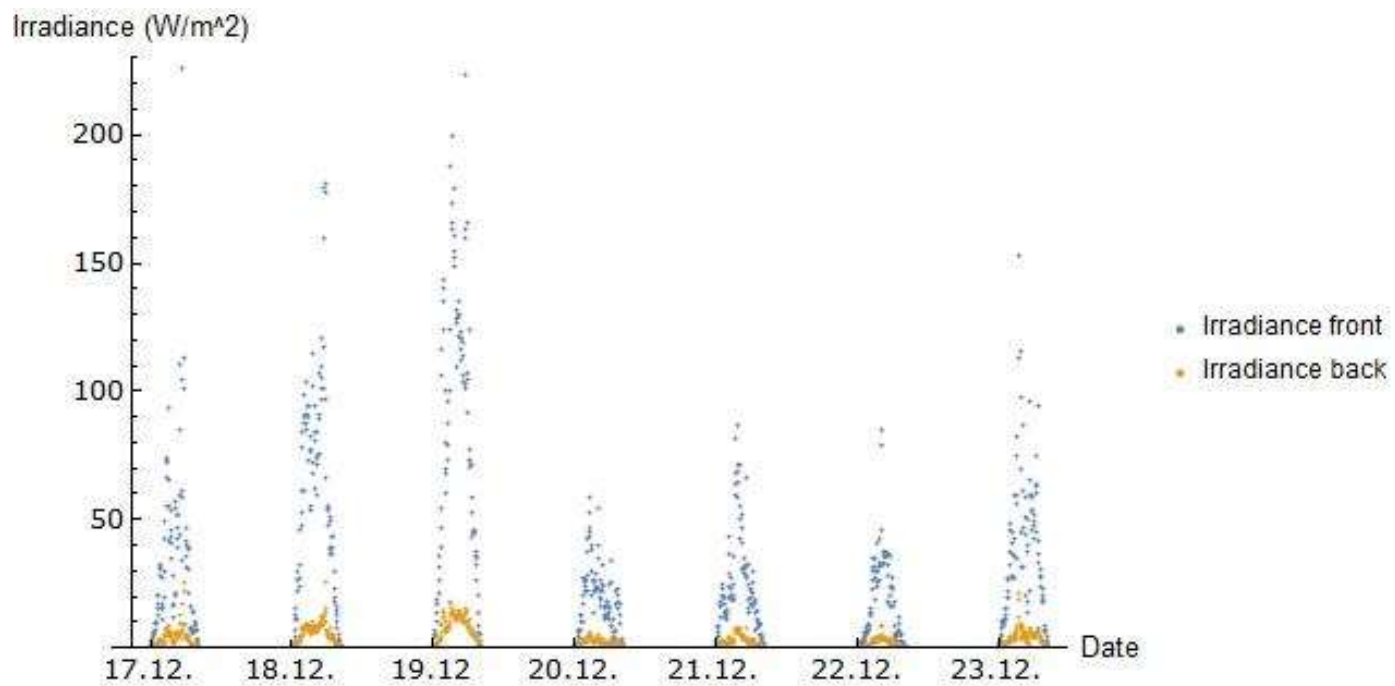


Figure 9:: Irradiance front and back for the period of 17.12.2019 until 23.12.2019

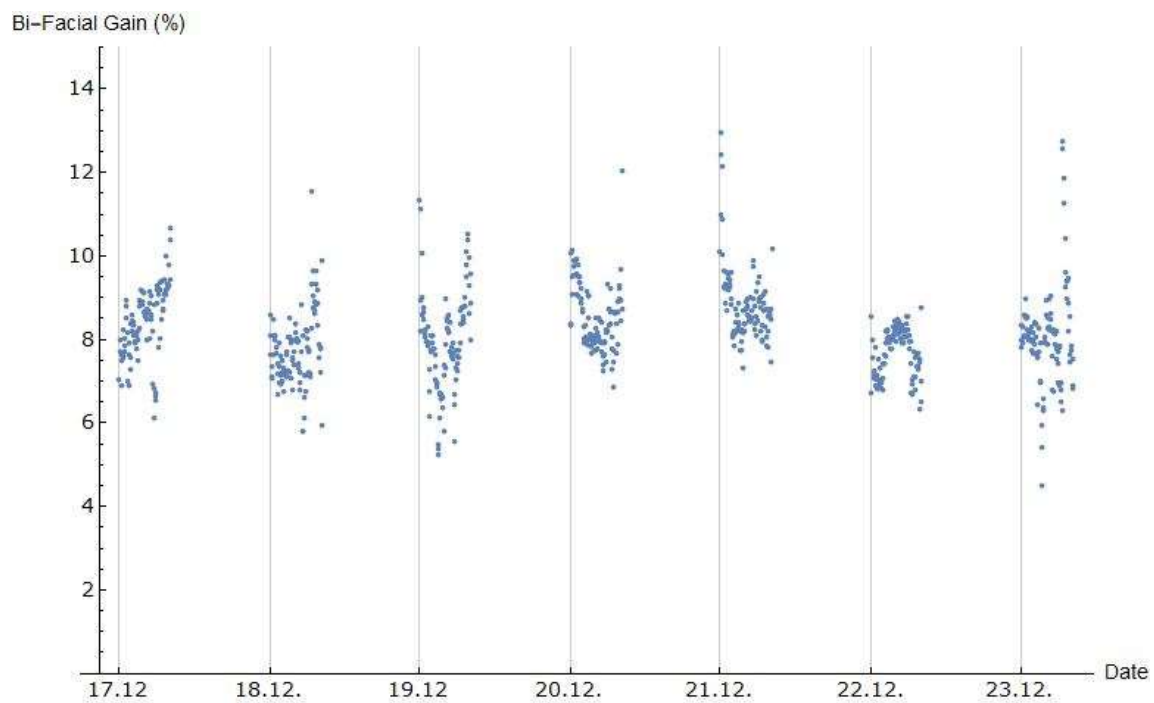


Figure 10: BFG for the time period of 17.12.2019 until 23.12.2019.
The vertical lines mark the first measurement of each day (at dawn)

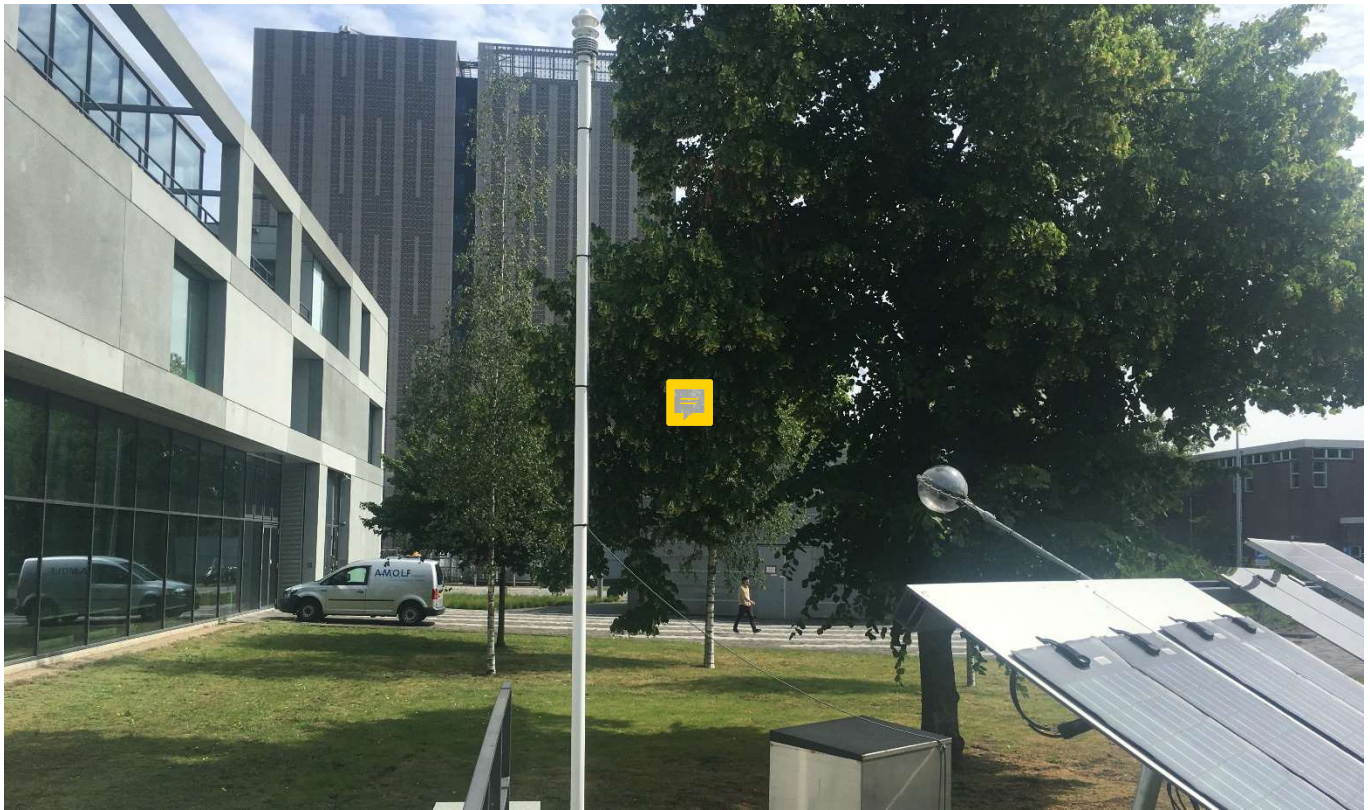
Plotting many days visualizes the trends related to the time of year, instead of simply the trends related to small-scale fluctuations, such as current weather events (see Figure 3). The vertical lines aid in understanding the trends of the BFG during this time. The BFG appear to follow a general parabolical shape throughout the day, being higher in the morning and evening than during high noon. This supports the finding of high BFG during lower irradiances in section 3.2.

The prominent spikes on the beginning of each day during summer equinox further strengthen the argument of high BFG occurring during low irradiance times in summer. The constant presence of one large spike in the morning but the absence of the same during evening times¹⁵ contradicts the idea that low-light hours during summer explain these highest observed BFGs.

Purely considering the steeper sun angle in summer does partly explain an overall higher BFG in Summer. This is because, in Amsterdam, a steeper sun angle in the morning means relatively direct sunlight South-East/South/South-West depending on the time of the year [14]. The back sensor of the LAD, which is facing diagonally towards the ground with a slight upwards North-inclination, would only be affected during dawn and dusk of the summer solstice.

Looking at the LAD exposure to the sun on site during the mornings from 11.06. until 15.06.2020 showed that these spikes most likely occurred due to reflections from the bright concrete wall and the windows at the wall of the AMOLF building facing the LAD. While this could be observed, the specific reflection was not photographed. Image 2 shows the wall and window front to the North-West of the LAD, which were identified to cause the reflection.

¹⁵ this occurred regularly throughout all summertime weekly graphs



Picture 2: LAD (right) relative to reflection surfaces of the AMOLF building (left), 17.06.2020, 11:35

3.4 Sun Angle Impact on BFG

To further investigate the influence of the sun angle on the BFG, the BFG of each day was plotted against the time distance to the zenith of each day¹⁶. This visualization puts the zenith of each day at the origin, to illuminate a potential connection between high BFG and sun angle. Figure 15 -18 plot of these values for the 14 days around summer solstice, fall equinox, winter solstice, and spring equinox respectively. Each differently colored plot marker represents a different day.

¹⁶ taking daylight saving time into account to center the graphs

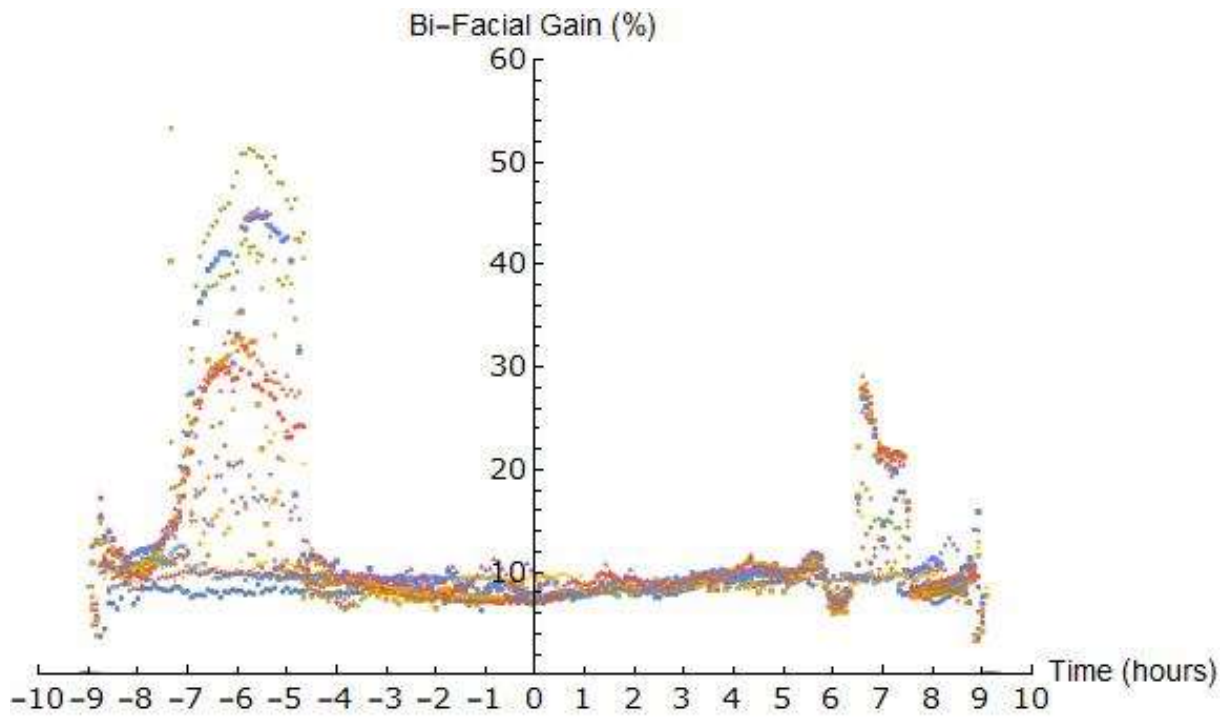


Figure 11: BFG vs. Hours to Zenith around summer solstice.
Each color represents one of the days from 20.06. until 03.07.2019.

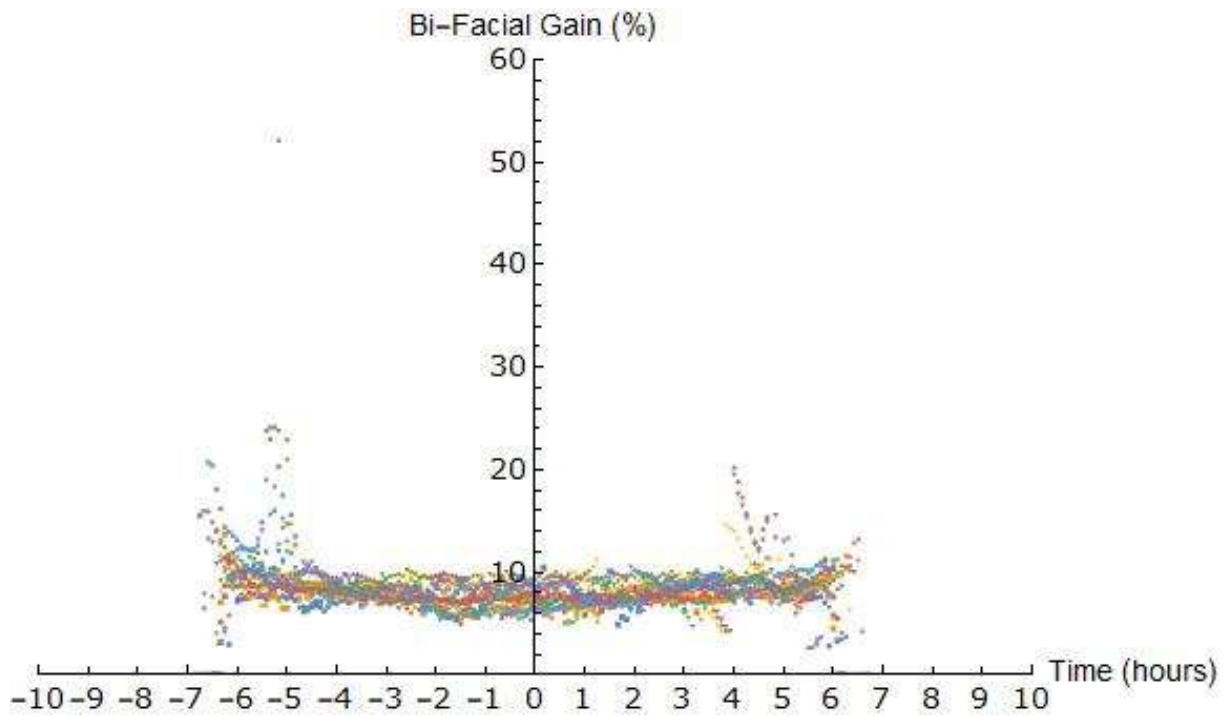


Figure 12: BFG vs. Hours to Zenith around fall equinox.
Each color represents one of the days from 19.09. until 02.10.2019.

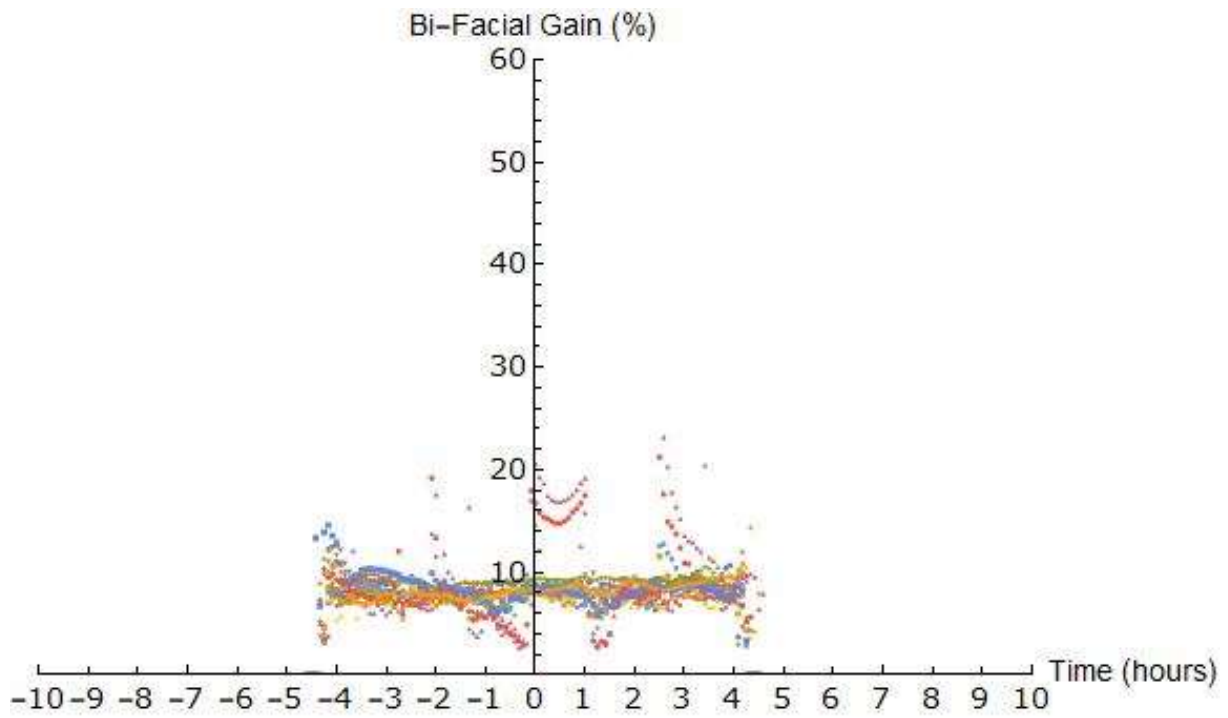


Figure 13: BFG vs. Hours to Zenith around winter solstice.
Each color represents one of the days from s 17.12. - 30.12.2019

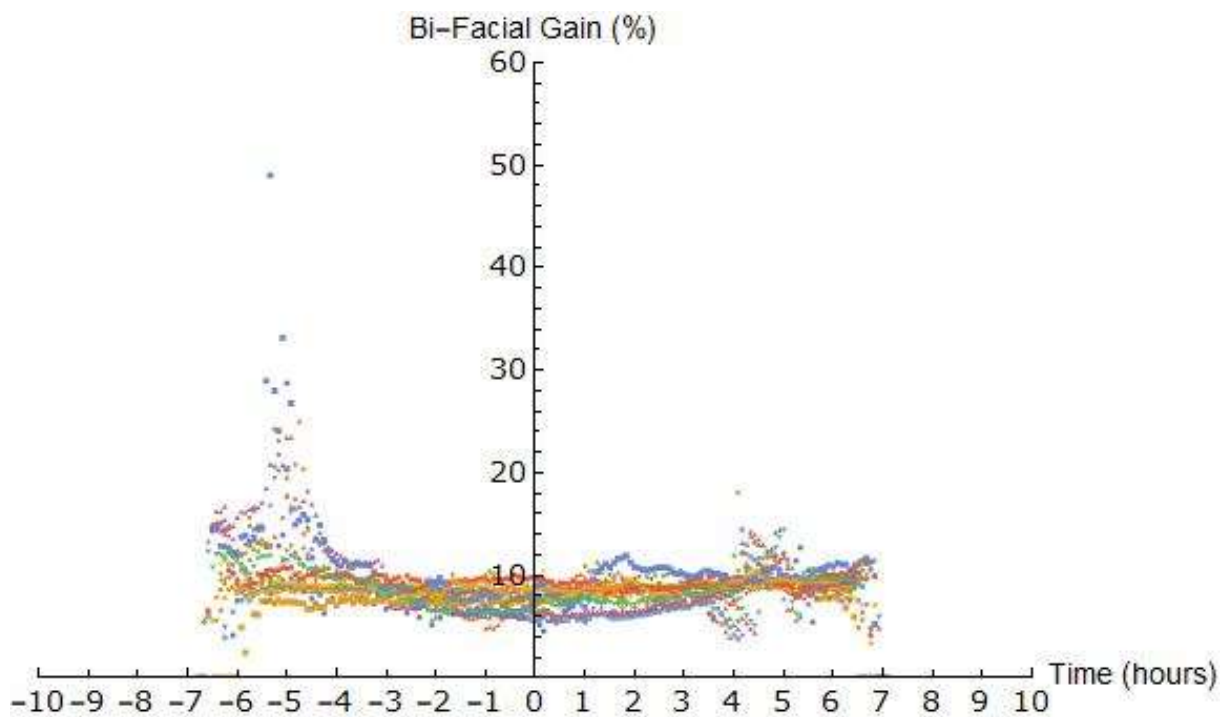


Figure 14: BFG vs. Hours to Zenith around spring equinox.
Each color represents one of the days from Days 17.03 - 30.03.2019.



Figure 11, 12, and 14 show a similar overall shape with tighter clusters closer to high noon and more extreme BFG at lower sun angles. This emphasizes a connection between low sun angle and high BFG during summer months, because high BFG exclusively occur during hours further away from the zenith. This is supported by Figure 13, which displays a less extreme pattern, resulting from lower sun angles in winter. The resulting higher BFG is thus impacted by low sun angles but is not exclusively linked to this factor.

Figure 15 contains an extreme – and for most days consistent – spike from negative eight to negative five. Since it occurs only in the morning, it cannot be due to sun angles. The shape supports the existence of repeated reflection occurring in the mornings for several weeks in summer which was mentioned in section 3.3 (Figure 8).

The major reflection spikes were observed to occur on site as a result of the AMOLF building, which is the only building with reflecting windows and brightly colored walls, that is positioned at a potential reflection angle relative to the LAD. As the largest structure in the immediate surroundings, it can be assumed that the reflections off of the AMOLF building result in larger and more consistent measurement deviations by the LAD.

The smaller dips and spikes in Figure 11-14 must have occurred due to similar factors in the surroundings, since any shape variation, which includes drastic instantaneous jumps and occurs repeatedly on several days at the same time, cannot be due to non-static factors such as weather. In particular, Figure 13 displays a vaguely parabolically shaped series of higher BFGs for three consecutive days, at 1 hour past zenith. This could have been caused by a tall post, positioned slightly southwest of the sensor, which covered the top sensor in shade for approximately 45 minutes every day in winter. This behavior in winter could not be observed at the time of writing thus remains hypothetical

3.5 BFG Day Weighted Average

To reduce the noise of the individual spikes, which were commonly occurring in the morning, the weighted average of BFG (equation 4) was taken over all nonzero measurements of each day of the year 2019. The following graphs show this weighted average for all days of 2019. Individual extreme spikes have been disregarded (see section 2.4).

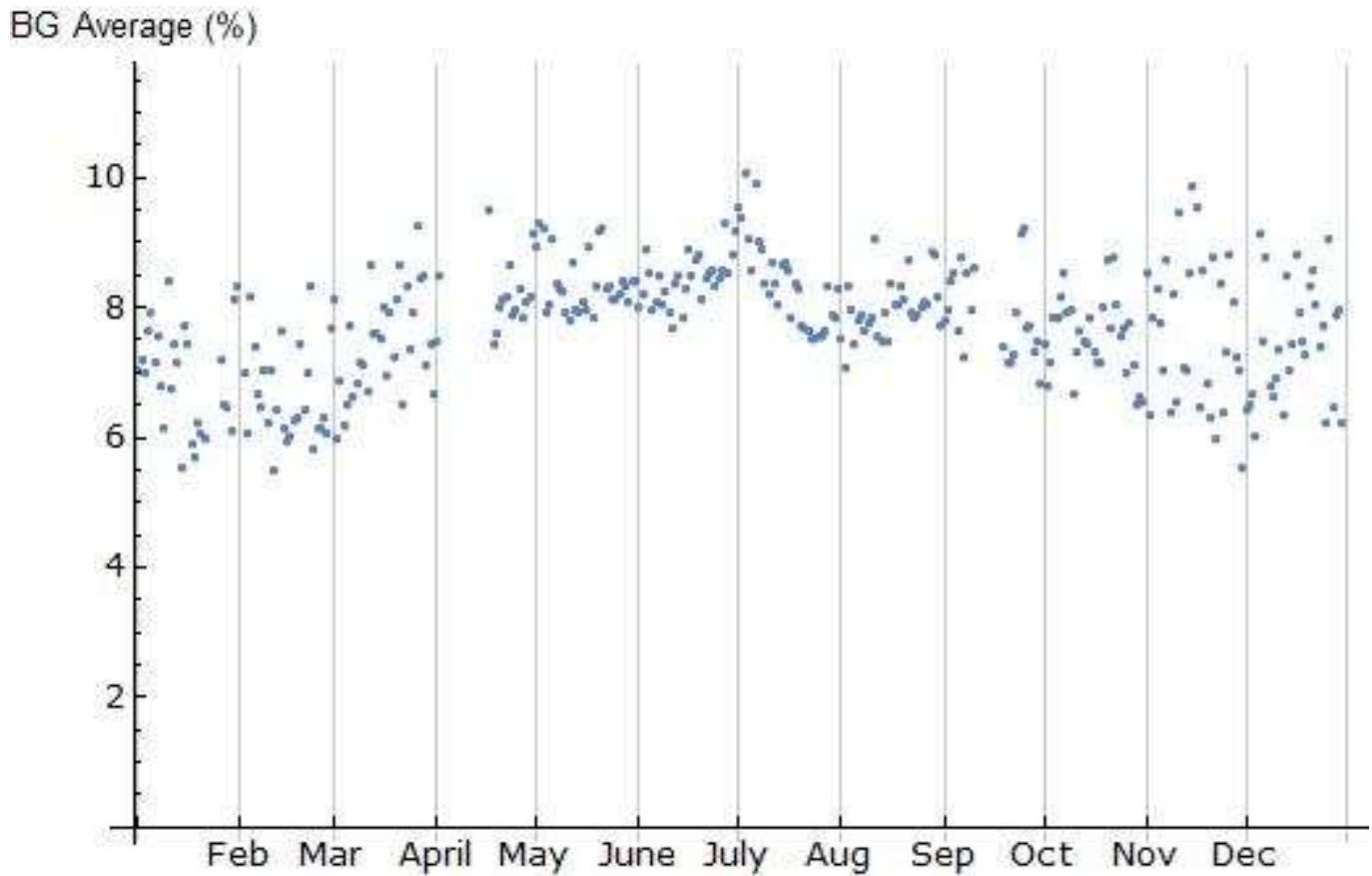


*Figure 15: Daily Weighted averages (Equation 4) of 2019.
Range is set to a maximum of 15% BFG to ignore disproportional spikes*

The shape of the cluster suggests overall higher BFGs in Summer, in accordance with Figure 5. A stronger fluctuation of average BFG in winter can be observed due to a wider spread of markers.

To further investigate the nature of daily weighted BFG averages, Figure 16 below plots the full range of Figure 15. The data input and the x-axis are identical, while the y-axis now contains the range from 0% to 36%.

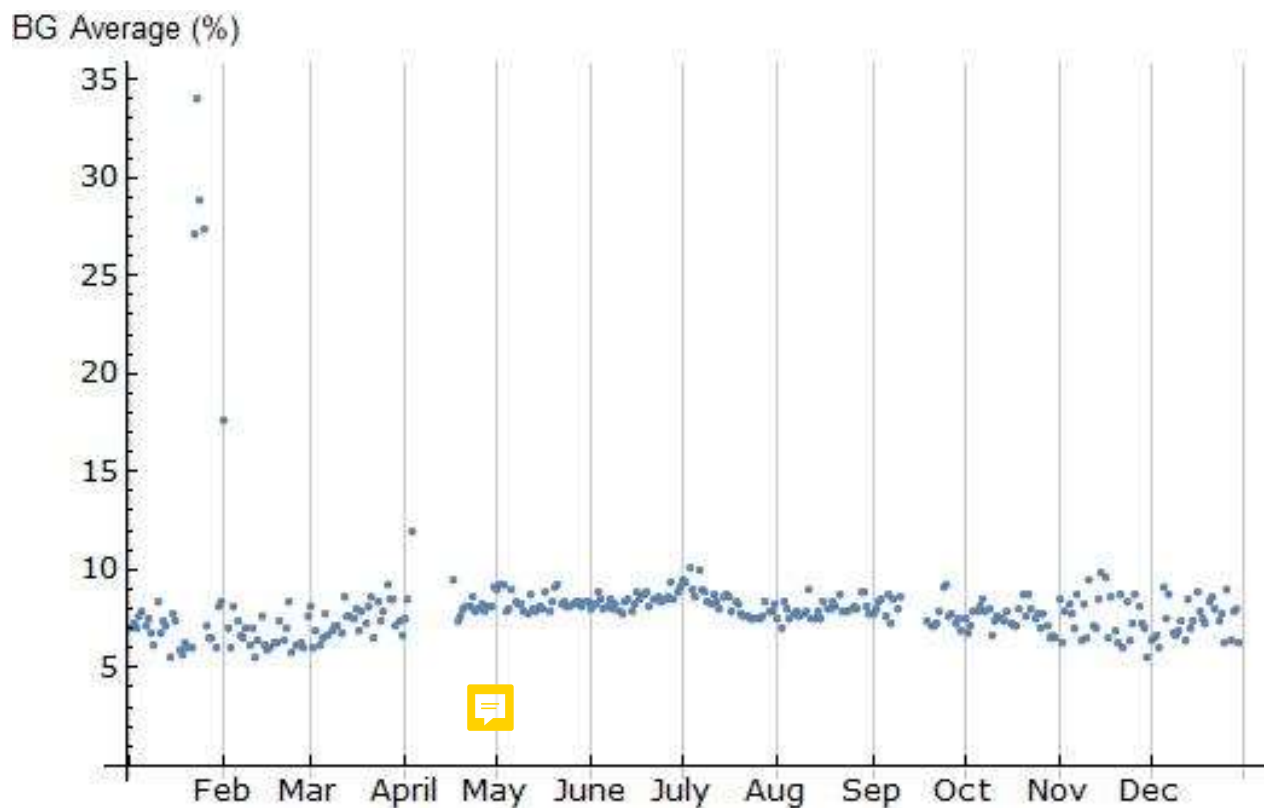


*Figure 16: Daily Weighted averages (Equation 4) of 2019.
Full range*

This action is equivalent to zooming out on the y-axis, where very high weighted averages of up to 35% in the beginning of the year become visible. These spikes do not coincide with the individual BFG extrema in Figure 5, which reached up to 81% BFG. The absolute day average maximum of 34% BFG occurred on the 23rd of January 2019 and was immediately followed by another 4 days of disproportionately high averages.

Figure 17 and 18 show the front and back irradiance, as well as the BFG on the 23rd of January, respectively.

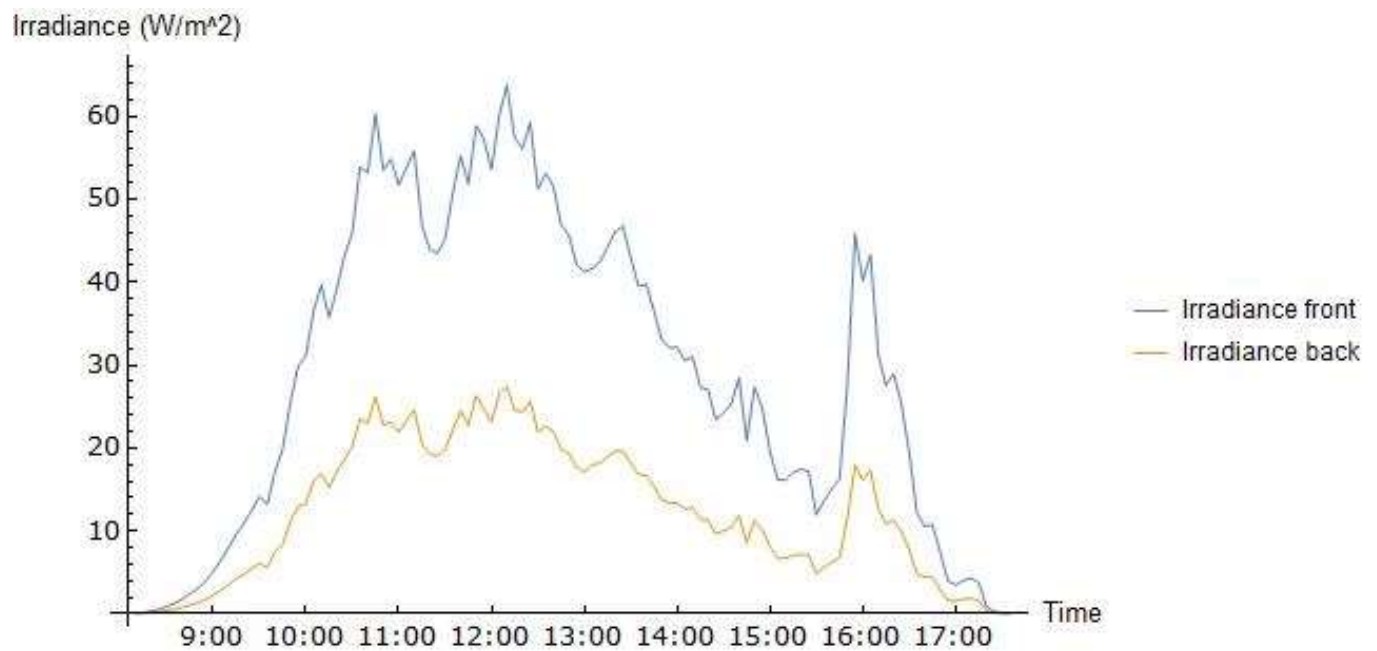


Figure 17: Irradiance front and back on 23.01.2019

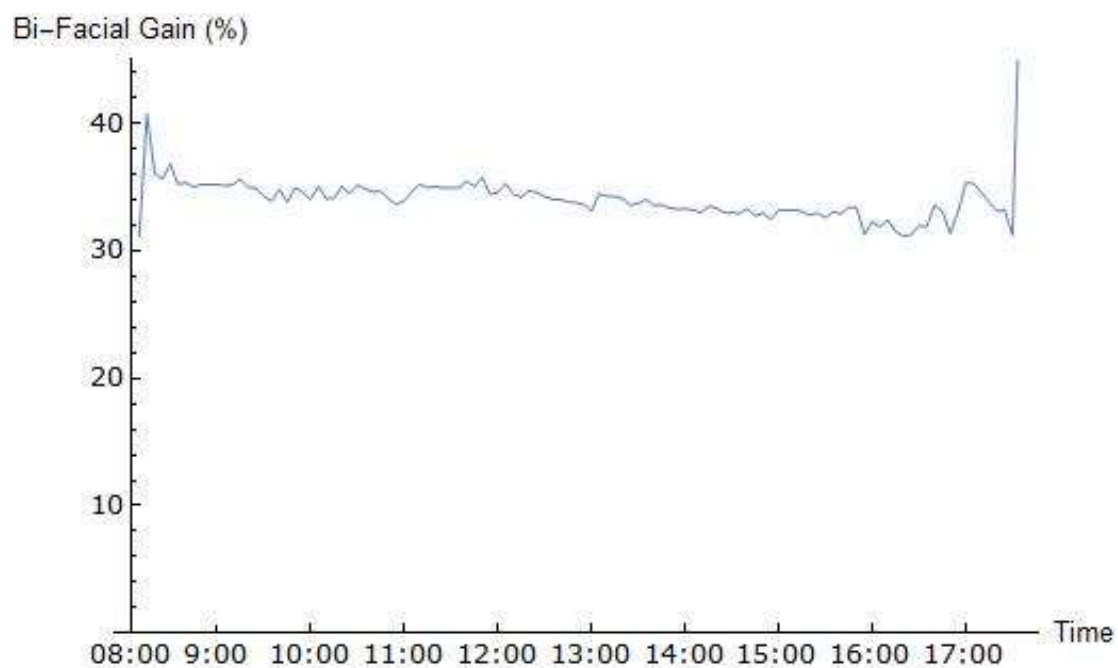


Figure 18: BFG on 23.01.2019

A consistent BFG of between 30% and 40% is visible in Figure 14, which numerically explains the weighted day average spike in Figure 16. The irradiance comparison shows an almost exactly proportional relation between back and front irradiance, with a proportionality constant of 0.43. The weather station measured no precipitation throughout the whole day, which refutes the possibility of unusually cloudy weather as an explanation for these extraordinary measurements. Considering unrelated factors, such as the lights of a parked car which were accidentally left on and pointed towards the LAD, are also contradicted by the fact that the irradiance increases and decreases around dawn and dusk. A promising explanation is the buildup of snow on top of the LAD on the 22nd of January, when the weather station recorded solid precipitation. This layer of snow deposited only on the top of the LAD, blocking a major portion of the direct irradiance and diffused the light to result in the very high BFG. Furthermore, snow coverage on the ground results in higher surface albedo in general, which would also increase BFG (see Figure 3).

4. Discussion


4.1 Reflection on data Analysis

Investigating the seasonal fluctuations of BFSP performance in the context of the results from section 3, several causes for seasonal BFG fluctuations have become evident. The impact of sun angle, weather impacts, and Irradiance fluctuation on the BFG were described and grounded in the data analysis:

Considering the overall increased efficiency of BFSP over MFSP, as shown in Figure 5, the average of 9.5% BFG in 2019 stresses the potential of BFSP. On average, a BFSP in Amsterdam will generate 9.5% more electricity than a MFSP. The BFG is typically (up to 50%) higher in summer, but does not decrease below a minimum of 4.5%, the lowest BFG in winter.

Since the daily BFG average and the Irradiance are both higher in summer (see section 3.1), the total advantage of BFSP over MFSP for application in the AMOLF solar field is therefore also higher in summer than in winter. A BFSP at AMOLF,

however, would not counteract lower power output in winter by having an increased BFG. Consequentially, the hypothetical BFSP would outperform MFSP by a larger degree during summer months than winter months.

The BFG fluctuations are small compared to the difference in irradiance between summer and winter. During winter months, the BFG is still around 7%, which could contribute a meaningful amount of electricity during the time of the year when most electricity is used [13]. 

The cause for the BFG spikes in Figure 8 was identified as reflection of the surroundings, when a specific sun angle resulted in a higher irradiation reaching the back of the LAD relative to the front. This can be easily classified as additional distortion when considering the BFG over a time period. However, reflection is a factor determined by the surroundings of the hypothetical BFSP. Considering the major impact surrounding albedo and reflections have on the BFG, the importance of strategic placement of a BFSP is clear. For example, in a scenario where a city would like to implement photovoltaics in an area with many tall buildings, the LAD could be used to determine when and where reflection spikes occur due to the surroundings and allow strategic positioning of the BFSP to boost efficiency during the desired times.

On the other hand, shadows by the same buildings or structures could result in an overall decrease of power output, despite the high BFG, since the total irradiance will be lower. No exact estimations to power decrease due to shadowing could be made at this point, since shade will usually block sunlight from reaching the front sensor and increase the BFG. Utilizing the LAD to determine the ideal spot for BFSP positioning mainly relies on the BFG, which will increase as sunlight is blocked from the front sensor.

The analysis of Figure 14 has shown that snow can result in a high BFG. This factor is increased for snow covered solar panels, as they do not benefit from the small, spherical surface area of the LAD which is less likely to be fully covered. Since the major share of private electricity use goes to heating [12], figuring out a way to

generate more electricity relative to a MFSP during winter, even while it is snowing, will benefit the relevance of BFSP in the future.

4.2 Limitations

This research relied exclusively on the data provided by the LAD and the weather station positioned at AMOLF. The reader must consider the location specificity of this research, and to what degree results will be applicable in a different setting. For the same reason, some factors such as reflection or shadows by buildings have inevitably distorted the data to some degree. The impact of reflectivity, condensation within the sphere, and light sensor calibration of the LAD are considered individually in this section:

The pmma hemispheres and the protective cover of the light sensors themselves contribute to the LAD internal reflectivity which distorts measurements. Looking at the position of the ring on which the LAD is mounted (Picture 1), relative to sensor 1 and 12 (top and bottom), it is a simple geometrical argument that the ring will have had no impact on either sensor: reflection from the ring could not hit sensors 1 or 12, and shadows cast by this ring also could not fall on them, as both were positioned on the sides of the dodecahedron which are outside of [overcast](#) region of the ring. The reflectivity of the pmma capsule and the protective cover of the sensors is assumed to have approximately matched the reflection losses a solar panel would be subject to due to its protective coating.

The relative uncertainty of the light sensors in the LAD is inversely proportional to irradiance and increases with temperature. Figure 19 below is a three-dimensional plot of the relative uncertainty of each sensor diode to the raw data [11].

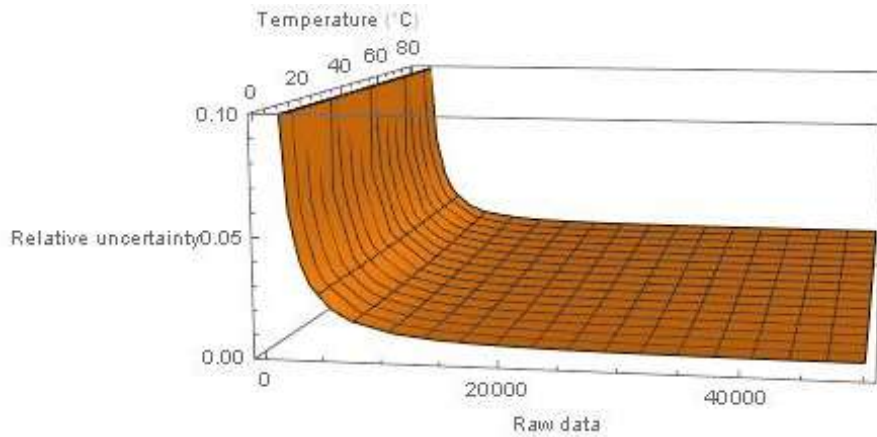


Figure 19: 3D plot of relative uncertainties, Raw sensor diode output, and temperature [11]

The front sensor raw data output ranges from 1500 bits as a daily average in winter to a daily average of 25000 bits in summer. Considering Figure 19, these measurements are subject to negligible fluctuations in summer, but are severely affected in winter, with an uncertainty larger than 0.1. The same large uncertainties can be expected during dawn and dusk of each day. The impact of uncertainties on BFG using low light measurements could therefore have been considerable. It was shown in the previous section that BFGs peak during these times of low intensities, thus increasing the arithmetic mean and weighted averages of BFG. Boogaarts [11] did not conclude whether or not these relative uncertainties tend to over- or underestimate the absolute measurements in low light, and therefore no final estimation of whether the BFG might have been positively or negatively affected can be made. An overestimation of BFG as light intensity decreases would have resulted in a higher BFG, as the back sensor would have taken measurements in less light than the front sensor. The opposite is true for an underestimation of the relative error.

Because humid air can get inside of the protection sphere and cool down on the pmma surface, condensation occurs frequently inside the LAD (see appendix b). A heating element was built into the central dodecahedron to minimize condensation and stabilize temperature. This heating element, however, was not positioned in a way which would allow it to heat up the inner surface of the hemispheres enough to prevent condensation entirely, since this can also decrease sensor accuracy (Figure 19). The LAD was therefore inherently subjected to a condensation error because of additional to light diffusion on the pmma surface. This presumably resulted in a decrease of contrast between measurements of all sensors. Since the data analysis considered only two sensors positioned on opposite faces of the dodecahedron, it can

be assumed that the occasional contrast reduction between sensor 1 and sensor 12 coinciding with the condensation was negligible.

Moreover, the overall decrease of measured irradiance due to condensation was assumed to be negligible, considering that this would occur on both faces to a similar degree. Condensation which resulted in some sensors receiving more light than others was ignored. Furthermore, large amounts of condensation which resulted in a small accumulation of water on the bottom of the protective sphere would have affected the back facing sensor despite being positioned diagonally towards the ground since it has a full 180-degree angle. This is because water accumulation on the bottom would result in less light reaching the back sensor, which would cause an underestimation of the BFG. No exact measurement offset estimation can be provided for this.

Due to technical problems which occurred in April and October 2019, the LAD did not have an output for several days which resulted in removing these timestamps and their corresponding measurements from the converted list. This allowed for correct calculations and plotting for the rest of the year but resulted in the evident holes in the presented graphs. Due to the number of datapoints immediately before and after the LAD failure, the seasonal trends which were investigated were not noticeably affected.

5. Conclusion

Data analysis of all 2019 LAD measurements showed an overall larger BFG in summer than in winter, coinciding with higher individual spikes. BFG above 15% occurred only at low irradiances (around 400 w/m^2), leading to the conclusion that the highest BFG will be obtained during low-light hours in summer. Weighted averages for each day of 2019 also showed higher BFG in summer. It can therefore be concluded that a BFSP will outperform MFSP to a larger degree in summer than in winter.

Major BFG spikes in the mornings of the week around summer solstice were identified as a result of reflection by the AMOLF building, supporting the hypothesis of reflections by immediate surroundings positively affecting the BFG. Disproportionally high BFG day averages in January occurred due to a combination of snow blocking light from reaching the top sensor and increased surface albedo. This proved the impact of seasonal-specific weather events on the BFG and provided additional understanding of BFSP performance in winter, during months where snowfall can occur on site.

Linking the results of this research to BFSP application, it should be mentioned that the BFG was very rarely determined to be below 4.5%, with an overall average of 9.5%. This could be used as an orientation when considering economic feasibility of BFSP relative to additional production cost. Until smart grids are widely implemented, merely producing a large amount of photovoltaic energy during peak hours in summer, where the BFG is highest, does not in itself manifest the superiority of BFSP to MFSP. It is relevant to add the relative performance during off-peak hours in summer, as well as additional generative potential at all times, to argue that BFSP are a very relevant and feasible improvement to MFSP.

Future research with measurements by the LAD could include BFG modelling for more than top to bottom orientation, utilizing the data of the remaining 10 sensors.

6. References

1. Bruckner T, Bashmakov IA, Mulugetta Y, Chum H, Navarro ADLV, Edmonds J, Faaij A, Fungtammasan B, Garg A, Hertwich E, et al. 2014 Energy Systems. In: Edenhofer O, Pichs-Madruga R, Sokona Y, Farahani E, Kadner S, Seyboth K, Adler A, Baum I, Brunner S, et al., editors. Climate Change 2014: Mitigation of Climate Change. Contribution of Working Group III to the Fifth Assessment Report of the Intergovernmental Panel on Climate Change. Cambridge (UK) and New York (NY): Cambridge University Press. p. 511-597.
2. Chang S, Parinov, I, & Topolov, V. 2014. Advanced Materials Physics, Mechanics and Applications (1st ed. 2014.). <https://doi.org/10.1007/978-3-319-03749-3>
3. Davis S. 2015. Solar System Efficiency: Maximum Power Point Tracking is Key. Powerelectronics. Available from <https://www.powerelectronics.com/technologies/solar/article/21863142/solar-system-efficiency-maximum-power-point-tracking-is-key>. Last accessed: 04.03.2020
4. Frank J, Rüdiger M, Fischer S, Goldschmidt J, Hermle M. 2012. Optical Simulation of Bifacial Solar Cells. Energy Procedia, 27(C), 300–305. <https://doi.org/10.1016/j.egypro.2012.07.067>
5. Giancoli DC. 2013. Physics for Scientists & Engineers with Modern Physics. Fourth Edition. London (UK): Pearson. 1426 p.
6. Kersten M. 2018. Outdoor solar cell performance - Improving a diffuseness measurement tool. [Bachelor Thesis] Amsterdam University College.
7. Marion B, MacAlpine S, Deline C, Asgharzadeh A, Toor F, Riley D, Stein J, Hansen C. 2017. A Practical Irradiance Model for Bifacial PV Modules. In: 2017 IEEE 44th Photovoltaic Specialist Conference (PVSC); 25-30 Jun 2017; Washington (DC). Piscataway (NJ): Institute of Electrical and Electronics Engineers (IEEE). p. 1537-1542. Available from: <https://www.nrel.gov/docs/fy17osti/67847.pdf> doi: 10.1109/PVSC.2017.8366263
8. Pollastri AL. 2019. A novel multi-directional light detector for modelling the cost-efficiency benefits of bifacial solar panels. [Bachelor Thesis]. Amsterdam University College
9. Shravanth Vasisht M, Srinivasan J, & Ramasesha S. 2016. Performance of solar photovoltaic installations: Effect of seasonal variations. Solar Energy, 131(C), 39–46. <https://doi.org/10.1016/j.solener.2016.02.013>
10. Sun X, Khan MR, Deline C, Alama MA. 2018. Optimization and performance of bifacial solar modules: A global perspective. APPL ENERG. [Internet]. [last accessed: 04.03.2020]; 212: 1601-1610. Available from: <https://www.sciencedirect-com.proxy.uba.uva.nl:2443/science/article/pii/S0306261917317567>
11. Boogaarts B. 2020. The use of a multi-directional light sensor for the simulation of bifacial solar panel performance [Bachelor thesis]. Amsterdam University College
12. U.S. energy Information administration (eia). 2013. Heating and cooling no longer majority of U.S. home energy use. Washington. Available from www.eia.gov/todayinenergy/detail.php?id=10271 [Last accessed: 17.06.2020]
13. U.S. energy Information administration (eia). 2011. Demand for electricity changes through the day. Available from Washington. www.eia.gov/todayinenergy/detail.php?id=10271 [Last accessed: 17.06.2020]
14. Chang T. 2009. The Sun's apparent position and the optimal tilt angle of a solar collector in the northern hemisphere. Solar Energy, 83(8), 1274–1284. <https://doi.org/10.1016/j.solener.2009.02.009>

7. Appendix

a)



Picture 2: AMOLF solar array with the LAD (center right).
17.06.2020, 11:30

b)



LAD: 11.02.2020, 13:00



LAD: 13.02.2020, 16:00



LAD: 18.02.2020, 16:00



LAD: 20.02.2020, 16:00



LAD: 27.02.2020, 17:00



LAD: 02.03.2020, 16:00



LAD: 04.03.2020, 15:00



LAD: 17.06.2020, 11:40

8. Acknowledgements

First and Foremost, I would like to thank my supervisors dr. Forrest Bradbury and dr. Bruno Ehrler, who provided me with this fantastic research opportunity and who always generously made time to help and give feedback. Thanks to these committed supervisors, this research could be continued during the challenging time of the COVID 19 pandemic 2020. Next, I would like to thank AMOLF, in particular all members of the hybrid solar cell group, where I was welcomed with open arms, despite the short-term nature of my internship. To conclude, let me express my gratitude to Prof. dr. Wim Sinke, who agreed to read and grade this thesis, and Bram Boogaarts, a fellow physics student at the Amsterdam University college, who was always available to answer questions regarding the sensor calibration. Thanks to these individuals, writing this Bachelor thesis was a highly enjoyable learning experience for which I am very grateful.